International Journal of Heat and Mass Transfer 273 (2027) 129721

Contents lists available at ScienceDirect

International Journal of Heat and Mass Transfer

journal homepage: www.elsevier.com/locate/ijhmt

Multiphase flow simulations for alkaline water electrolysis: a parametric study towards cell design optimisation

Kevin Van Droogenbroek [a,*], Ahmed Aissa Berraies [a], Hamed Abedini [b], Benoit Scheid [c], Joris Proost [a]

[a] Louvain Research & !nnovation Centre for Sustainable Process Engineering (ReC!PE), UCLouvain, Louvain-la-Neuve, Belgium
[b] John Cockerill Hydrogen, Seraing, Belgium
[c] Transfers, Interfaces and Processes, Université Libre de Bruxelles, Brussels, Belgium

ARTICLE INFO

Keywords:
Water electrolysis
Multiphase flow
Mixture model
Gas accumulation
Outlet configuration

ABSTRACT

In this work, multiphase computational fluid dynamics (CFD) simulations are used to analyse and optimise alkaline water electrolysis cells. A quantitative methodology is proposed to compare different cell geometries through the introduction of a representative parameter that captures the efficiency and uniformity of gas removal as a function of current density. Cell configurations that limit gas accumulation while at the same time promoting homogeneous gas evacuation are identified. The influence of the positioning of gas outlet channels is first investigated, as it plays a crucial role in efficient bubble removal. Our results show that these outlet locations strongly affect multiphase transport. In addition, the impact of the porous transport layer (PTL) is examined. The simulations indicate that more open structures, such as knitted mesh-type spacers, promote more balanced gas outflows compared to highly porous foam structures within the configurations considered. These results highlight the importance of adapting electrolyser cell design to the characteristics of the type of PTL used. In this respect, this paper also provides guidelines for a more optimal integration of advanced PTL into prototype alkaline water electrolysis cells.

1. Introduction

The transition from fossil fuels to renewable energy sources is an essential requirement to meet the ambitious decarbonisation targets set by the international community [1]. Electricity is expected to play a central role in reducing carbon emissions by 2050, even though the direct electrification of certain sectors, such as heavy industry, long-haul transportation and energy storage applications, remains challenging [2–4]. Owing to its remarkable flexibility, its ability to be efficiently converted into other energy carriers and its suitability for long-term storage, hydrogen is considered a promising solution to meet these specific needs [2]. When produced using renewable electricity, hydrogen is referred to as sustainable. As a result, among the available production routes, water electrolysis currently stands out as the most sustainable technology for hydrogen generation [5].

Alkaline water electrolysis (AWE) has emerged as the most promising and mature way of producing sustainable hydrogen, as it does not rely on the use of scarce and expensive materials, contrarily to proton exchange membrane (PEM) technologies [6]. For this reason, AWE presents a lower capital cost per kilowatt of electricity [7]. However, it still suffers from a lower hydrogen production rate per electrode area as compared to PEM electrolysis [8]. The shift from traditional gap cells to zero-gap cells, wherein 3D structures are used as electrodes, appears to be part of the solution thanks to the higher available surface area [9,10]. Bubble evacuation remains a challenge though, as bubbles may be trapped within the complex porous structure of the electrodes, and then reduce the overall efficiency [11]. Recent experimental studies in our group have shown that the electrochemical performance of alkaline electrolysers can be improved to reach PEM-like behaviour, with voltages lower than 2 V at current densities up to 2 $A{\cdot}cm^{-2}$ [12]. This remarkable performance was attributed to the use of flow-engineered laterally-graded bi-layer foam electrodes operating under a forced upwards electrolyte flow. This novel electrode geometry combines a fine porous layer for maximum hydrogen production and a coarse porous transport layer (PTL) for efficient bubble removal. The pressure gradient between the two layers generates a lateral transfer from the catalytic

* Corresponding author.
E-mail address: kevin.vandroogenbroek@uclouvain.be (K. Van Droogenbroek).

https://doi.org/10.1016/j.ijheatmasstransfer.2026.129721
Received 25 June 2026; Received in revised form 12 September 2026; Accepted 5 October 2026
Available online 8 October 2026
0017-9310/© 2026 The Author(s). Published by Elsevier Ltd. This is an open access article under the CC BY-NC-ND license (http://creativecommons.org/licenses/by-nc-nd/4.0/).

layer to the PTL, which promotes bubble evacuation and thereby reduces the Ohmic resistance of the cell. Computational fluid dynamics (CFD) simulations have been combined with experimental characterisation in order to validate this behaviour [12,13].

In industrial-scale systems, some efforts are still required to make industrial AWE systems more efficient and competitive with respect to other hydrogen production techniques [14]. In the last years, the emergence of zero-gap electrolysers with forced flow [15] has led to some improvement as compared to traditional electrolysers, i.e. with gap cells operating under natural convection [16], but operational cell voltages on the order of 2 V at 2 A·cm^{-2} have barely or never been observed [17,18]. The most recent systems typically use perforated 2D plates as active electrodes and elastic elements as PTL to maintain the electrical contact between the current collector plates and the electrodes [19,20]. The poor electrochemical performance reported at industrial level, as compared to lab-scale setups, has been attributed to a non-optimal distribution of the electrolyte within the anodic and cathodic compartments [21]. Indeed, the vast majority of AWE stacks are made of circular cells with small inlet and outlet channels [20, 22–24], leading to the formation of jet flows at the cell entrance [21,22]. For this reason, the electrolyte will not fill the cell uniformly, with some dead or stagnant zones that are not flushed by the electrolyte. On top of this, flow recirculation can occur, so that electrogenerated gas bubbles are not evacuated correctly and remain trapped within the cell. Based on these observations, AWE manufacturers started to consider new cell designs that distribute the electrolyte more homogeneously while trying to remove the bubbles in an optimal way [25,26]. Once again, numerical simulations appear to be the adequate tool to test and compare a wide range of cell configurations.

As a first step, single phase CFD models are relevant to simulate electrolyte flow within intricate 3D structures [9,10,12,13] or at cell level [21,27] as they allow to develop preliminary designs and understand flow behaviour in conjunction with electrochemical testing. However, these relatively simple models do not account for the presence of gas bubbles, although the latter do play a significant role in the overall flow distribution and efficiency of the cell. Multiphase flow models tackle this issue as the gas-electrolyte interaction is considered. Due to the numerical complexity of the existing models, most research work on this topic focus on gas evolution along (planar) electrodes at lab-scale level [28–34]. More recent studies highlight the importance of geometrical details on gas accumulation and flow distribution at industrial-scale level [22,25,32]. In addition, recent multiphase CFD investigations have started to introduce performance indicators for evaluating electrolyser operation and comparing design concepts [33, 34]. Nevertheless, most studies remain focused on the analysis of specific geometries or operating conditions, while general quantitative methodologies enabling systematic comparison and optimisation of cell designs based on gas-distribution characteristics remain scarce. The development of such methodologies is therefore essential to support the design of next-generation alkaline electrolysers.

The main objective of this work is to extend the methodology developed in our previous study [21] by performing multiphase flow simulations and develop a strategy to find an optimal AWE cell design. A gas outlet uniformity parameter is defined to compare different configurations on the same ground. The optimal geometry is the one that prevents gas accumulation while homogeneously evacuating it from the cell. The effect of the porous transport layer is also assessed to confirm whether a well-distributed electrolyte flow also leads to well-evacuated gas.

The paper is further organised as follows: Section 2 details the governing equations and the computational workflow established to simulate multiphase flow within a prototype alkaline water electrolysis cell. In Section 3, the results of the simulated multiphase model are presented and alternative cell configurations are defined and compared. Based on the most promising designs, the choice of the adequate porous transport layer is also discussed. Finally, Section 4 summarises the main conclusions and perspectives related to this study.

2. Materials and methods

In this section, we present the computational workflow developed to create the numerical model and simulate multiphase flow within a prototype alkaline water electrolysis cell. We first describe the cell geometry, then define the set of governing equations and the related boundary conditions and finally present the numerical methods used to solve the CFD equations.

2.1. Cell geometry

Fig. 1 shows the cathodic half-cell geometry used as reference in this work. The cell consists of a flat cylinder of 280 mm diameter and a thickness of 4.3 mm, encompassing a knitted mesh which serves as porous transport layer (PTL). The geometric details of the knitted mesh-type spacer can be found in [21]. Forced electrolyte supply is ensured by two inlets with circular shape having 2.5 mm diameter each. The inlets are located in the lower-left region of the cell, while gas-electrolyte evacuation occurs through five outlets, also circular, having 3 mm diameter each. Three outlets are positioned diametrically opposite the inlets in the upper-right region, and two additional outlets are placed on the left hand-side of the cell. The angular positions and mutual spacing of the inlets and outlets are indicated in Fig. 1. In what follows, the outlet channels will be numbered from left to right, from outlet 1 to outlet 5. Next to this, Fig. 2 shows how the five exit channels have been connected together to evacuate the flow into one shared outlet.

2.2. Multiphase flow

The electrolyte is a 30 wt% potassium hydroxide (KOH) solution operating at a temperature and pressure of 80°C and 16 bar, respectively. The electrogenerated gas is hydrogen (H_2) and it is assumed to be produced homogeneously on the electrode surface (front wall), as shown in Fig. 1. Indeed, since the flow field material (knitted mesh or foam) connects the electrode homogeneously to the bipolar plate and since the cell configuration is zero-gap, there is no electrolyte between the electrodes and the diaphragm, meaning that the current is distributed uniformly on the electrode surface and consequently, the hydrogen is homogeneously generated on it. The density of hydrogen can be

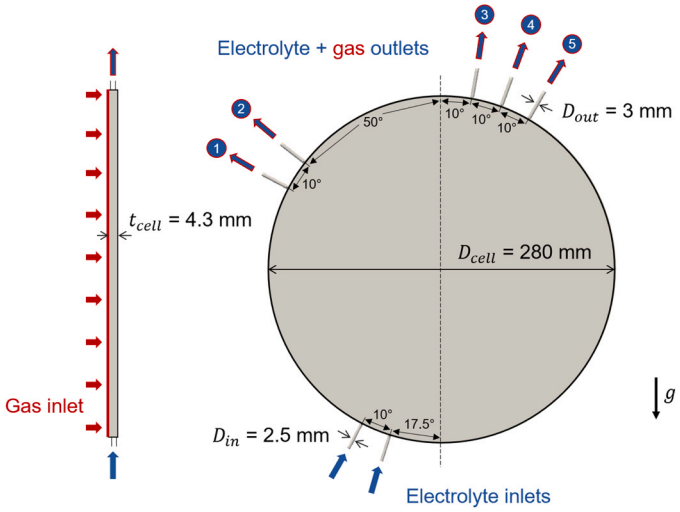


Fig. 1. Cathodic half-cell used as a reference configuration for the simulations from side (left) and front (right) view. The electrode is located outside the computational domain (front wall), where gas is being produced. The knitted mesh used as a PTL is modelled by implementing a Darcy-Forchheimer drag force in ANSYS Fluent.

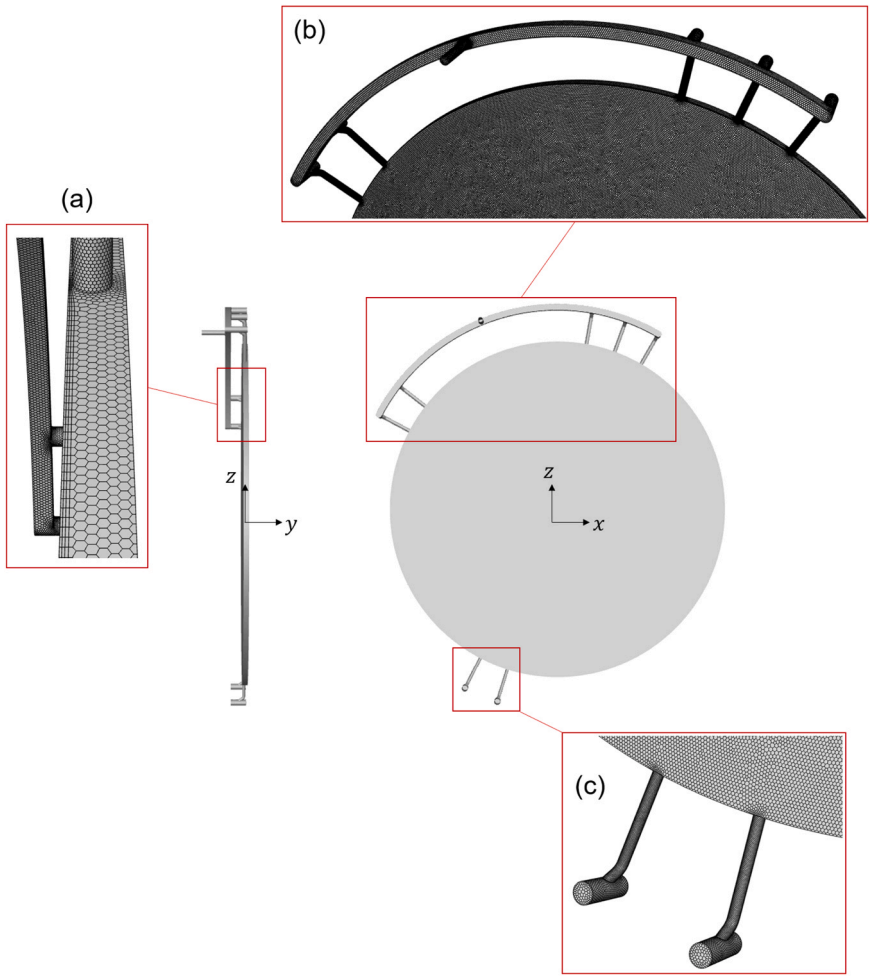


Fig. 2. Side (left) and front (right) views of the computational domain considered for the reference cell. Zoom-in on (a) the refined region where gas is being produced, (b) the shared outlet channel and (c) the two inlet channels.

calculated according to the ideal gas law:

$$\rho_g = \frac{p \cdot M_g}{R \cdot T} \tag{1}$$

with p the operating pressure, M_g the molar mass of the gas (i.e. $M_g = 2{\cdot}10^{-3}$ kg·mol^{-1}), R the universal gas constant (8.3145 J·K^{-1}·mol^{-1}) and T the operating temperature in degree Kelvin. The gas viscosity is computed using the Sutherland's formula [35]:

$$\mu_g = \mu_0 \cdot \left(\frac{a}{b}\right) \cdot \left[\frac{T}{T_0}\right]^{3/2} \tag{2}$$

$$a = 0.999 \cdot T_0 + C \tag{3}$$

$$b = 0.999 \cdot T + C \tag{4}$$

where μ_0 is the reference viscosity of the gas at reference temperature $T_0 = 293.15$ K and C is the Sutherland's constant. In the case of hydrogen, $\mu_0 = 0.88{\cdot}10^{-5}$ Pa·s and $C = 72$ K [35].

In order to describe the two-phase dynamics within the electrolysis cell, a mixture model formulation for incompressible flow [36] is used. Each phase is treated as an interpenetrating continuum within an Eulerian framework. Following the methodology developed by Rajora et al. [28,29] and van der Does et al. [34], this model remains valid as long as the continuous and dispersed phases are in dynamic equilibrium. This implies that there is no relative acceleration between the two phases, which is a reasonable assumption for small bubbles that arise in alkaline water electrolysis. Furthermore, the bubbles are assumed to be spherical with a constant bubble diameter $d_b = 100$ μm [30,37]. This assumption corroborates experimental studies [38–40], in which the impact of coalescence on hydrogen bubble size distribution has been studied. In particular, these studies show that the mean size of the bubbles increases by increasing the current density, while coalescence events (hence the variance of the size distribution) decrease as the KOH concentration increases. In particular, for current densities of around 2 A·cm^{-2} and the highest KOH concentrations tested, the bubble size is indeed about 100 μm in diameter. The amount of bubbles is defined by the gas fraction α and the mixture properties are weight-averaged based on this fraction. In that regard, the continuity equation for the incompressible mixture is the following:

$$\frac{\partial \rho_m}{\partial t} + \nabla \bullet (\rho_m \boldsymbol{v_m}) = 0 \tag{5}$$

where $\rho_m = (1-\alpha)\cdot\rho_l + \alpha\cdot\rho_g$ is the mixture density and $\boldsymbol{v_m}$ represents the volume-averaged velocity of the mixture. The latter is defined as $\boldsymbol{v_m} = (1-\alpha)\cdot\boldsymbol{v_l} + \alpha\cdot\boldsymbol{v_g}$, with $\boldsymbol{v_l}$ and $\boldsymbol{v_g}$ the liquid and gas velocities, respectively. The momentum equation for the mixture is obtained by combining the individual momentum equations for each phase:

$$\frac{\partial}{\partial t}(\rho_m \boldsymbol{v_m}) + \nabla \bullet (\rho_m \boldsymbol{v_m^2}) = -\nabla p + \nabla \bullet \mu_m \left[(\nabla \boldsymbol{v_m} + \nabla \boldsymbol{v_m^T}) - \frac{2}{3}\nabla \bullet \boldsymbol{v_m} \boldsymbol{I}\right] + \rho_m \boldsymbol{g} + \boldsymbol{S} - \nabla \bullet \left((1-\alpha)\rho_l \boldsymbol{v_{dr,l}^2} + \alpha \rho_g \boldsymbol{v_{dr,g}^2}\right) \tag{6}$$

where $\mu_m = (1-\alpha)\cdot\mu_l + \alpha\cdot\mu_g$ is the mixture viscosity, $\boldsymbol{g}$ accounts for gravity, $\boldsymbol{S}$ encompasses all the source terms present in the model and $\boldsymbol{v_{dr,k}} = \boldsymbol{v_k} - \boldsymbol{v_m}$ is the drift velocity for secondary phase k (with $k = l, g$). An algebraic slip formulation is used to define the relative velocity between the two phases, also referred to as the slip velocity $\boldsymbol{v_s}$, following Manninen et al. [41]:

$$\boldsymbol{v_s} = \boldsymbol{v_g} - \boldsymbol{v_l} = \frac{\rho_g d_b^2}{18\mu_l f_D}\frac{(\rho_g - \rho_m)}{\rho_g}\left(\boldsymbol{g} - (\boldsymbol{v_m}\bullet\nabla)\boldsymbol{v_m} - \frac{\partial \boldsymbol{v_m}}{\partial t}\right) \tag{7}$$

where the drag function f_D is described based on the Schiller-Naumann model [42]:

$$f_D = \begin{cases} 1 + 0.15\cdot \mathrm{Re_r}^{0.687}, & \mathrm{Re_r} \le 1000 \\ 0.0183\cdot \mathrm{Re_r}, & \mathrm{Re_r} > 1000 \end{cases} \tag{8}$$

with $\mathrm{Re_r}$ the relative Reynolds number, defined as $\mathrm{Re_r} = \rho_l|\boldsymbol{v_s}|d_b/\mu_l$. Next to this, the surface tension coefficient is assumed to be constant: $\sigma_s = 0.081\ \mathrm{N\cdot m^{-1}}$ [43].

Due to the small inlet diameter D_{in} and based on the imposed electrolyte flow rate, turbulent jet flows (Reynolds number Re~2300) are expected to develop at the cell entrance [21,44]. The shear-stress transport (SST) k-ω turbulence model is chosen to model the turbulent flow, since it combines the k-ε model, which operates well in the free-stream regions, and the k-ω model, which shows good accuracy in the boundary layer region close to the walls using a blending function [45].

For the initial state, a preliminary single-phase steady-state simulation is performed to ensure that the cell is filled with electrolyte. The governing Eqs. (5) and (6) are complemented with a set of boundary conditions. The boundary of the fluid $\partial\Omega$ is partitioned into three types: inflow boundaries (Γ_{in}), an outflow boundary (Γ_{out}) and rigid walls (Γ_w). The two electrolyte inlets are defined as inflow boundaries and an inlet velocity is prescribed to match the constant inlet flow rate Q considered in this work. The gas fraction is fixed to zero at the electrolyte inlets. At the outlet, a homogeneous Neumann condition, characterised by zero traction, is enforced. Note that numerical back-flow at the outlets is reduced by connecting the outlets with a shared channel (see Fig. 2). At the walls, a no-slip boundary condition is imposed, setting the mixture velocity to zero:

$$\boldsymbol{v_m} = 0 \qquad \text{on } \Gamma_w \tag{9}$$

At the electrode surface, where gas is electrochemically produced, a volumetric mass source is applied for the gas phase through a user-defined function (UDF). Following the studies of Zarghami et al. [30], the source is located in a thin layer adjacent to the front wall, whose thickness is fixed to $t_{layer} = 100\ \mu\mathrm{m}$ in order to match the characteristic bubble size. The UDF identifies the computational cells belonging to this layer based on their centroid position and assigns a homogeneous volumetric source term within this region, while the source is set to zero elsewhere. The volumetric source term $S_{g,in}$ (expressed in $\mathrm{kg\cdot m^{-3}\cdot s^{-1}}$) is calculated according to Faraday's law:

$$S_{g,in} = \frac{j}{z\cdot F}\cdot M_g \cdot \frac{1}{t_{layer}} \tag{10}$$

where j is the current density, $z = 2$ is the number of electrons exchanged during the reaction and F is the Faraday constant ($96{,}485\ \mathrm{s\cdot A\cdot mol^{-1}}$). In the UDF implementation, the total Faradaic mass production rate is first computed from the electrode surface area and then normalised by the volume of the source layer in order to obtain a volumetric source term consistent with Eq. (10). The hypothesis of a homogeneous gas production is made [30,32], so that j is considered constant over the whole electrode surface, leading to a uniform gas generation rate inside the source layer. The derivative of the source term with respect to the transported variable is set to zero, so that the source is treated explicitly, which improves numerical stability.

2.3. Darcy-Forchheimer approximation

Following the methodology developed in [21], the integration of porous media as PTL within the cell is done implicitly by adding a momentum source term to the standard momentum equation, denoted S_i, which treats the 3D structure as a continuous porous zone. This accounts for the pressure drop caused by the porous medium [46]. This source term is composed of two parts: a viscous loss term (Darcy's law) and an inertial loss term (Forchheimer's law). It is modelled by implementing the Darcy-Forchheimer law [47]:

$$S_i = -\left(\sum_{j=1}^{3} D_{ij}\mu_m v_{m,j} + \sum_{j=1}^{3} F_{ij}\frac{1}{2}\rho_m |v_m| v_{m,j}\right) \tag{11}$$

The indices $i = 1, 2, 3$ and $j = 1, 2, 3$ refer to the three dimensions of space. In particular, for an isotropic medium, this equation becomes:

$$\boldsymbol{S} = -\left(\frac{1}{k_1}\cdot\mu\cdot\boldsymbol{v_m} + k_2\cdot\rho\cdot|\boldsymbol{v_m}|\boldsymbol{v_m}\right) \tag{12}$$

with k_1 the permeability of the medium (associated with the viscous resistance tensor D_{ij}) and k_2 the inertial resistance factor (related to the inertial resistance tensor F_{ij}). These two parameters, which define the porous medium properties, must be supplied as inputs to the model.

Three types of PTL will be compared in this work: a knitted mesh-type spacer ($k_1 = 1.26\cdot10^{-5}\mathrm{m^2}$ and $k_2 = 10.29\ \mathrm{m^{-1}}$), a 3000 μm foam ($k_1 = 94.76\cdot10^{-9}\mathrm{m^2}$ and $k_2 = 290.46\ \mathrm{m^{-1}}$) and a 450 μm foam ($k_1 = 2.62\cdot10^{-9}\mathrm{m^2}$ and $k_2 = 2437.31\ \mathrm{m^{-1}}$), that were used in our previous studies [9,12,21]. The parameters k_1 and k_2 were obtained from pressure drop calculations on the explicit structures, that will be considered isotropic in what follows since their orientation only slightly modifies the flow behaviour, especially in the velocity range of interest [13,21]. The geometric details of each type of PTL are shown in Fig. 3. As observed, the knitted mesh offers a relatively open structure with nickel wires exhibiting a spacing ~6 mm, while the foams are much denser, with their solid struts occupying most of the space. This translates to a difference in porosity with 98% for the knitted mesh, 94% for the 3000 μm foam and 85% for the 450 μm foam.

2.4. Numerical methods

The following setup is used to perform the simulations. The considered electrolyte (liquid phase) has a density $\rho_l = 1208.39\ \mathrm{kg\cdot m^{-3}}$ and a dynamic viscosity $\mu_l = 10^{-3}\ \mathrm{Pa\cdot s}$ [48]. An inlet volumetric flow rate of $0.225\ \mathrm{l\cdot min^{-1}}$ is prescribed per cell inlet, corresponding to a velocity of $0.195\ \mathrm{m\cdot s^{-1}}$ per inlet. The electrogenerated gas is hydrogen (gas phase) and it has a density $\rho_g = 1.09\ \mathrm{kg\cdot m^{-3}}$ and a dynamic viscosity $\mu_g = 0.97\cdot10^{-5}\ \mathrm{Pa\cdot s}$ at the temperature and pressure considered in this work (see Eqs. (1) and (2)). Both phases are considered to be incompressible and isothermal. A standard pressure outlet boundary condition is specified at the domain outlet, with a gauge pressure of 0 Pa. A no-slip boundary condition is applied to the walls, including the front and back faces and the inlet and outlet channels. The k_1 and k_2 values obtained from previous pressure drop calculations on explicit porous structures are prescribed to the interior of the cell, as well as the porosity value of each PTL structure.

The discretised continuity and momentum Eqs. (5) and (6) are solved using the pressure-based solver in ANSYS Fluent. The SIMPLE (Semi-Implicit Method for Pressure Linked Equations) algorithm is implemented for pressure-velocity coupling. This segregated algorithm solves the momentum and pressure-correction equations sequentially in an iterative manner. This method provides a robust and memory-efficient solution as compared to the coupled solver. Convergence of the solution is ensured by monitoring the gas fraction at the outlets, and the

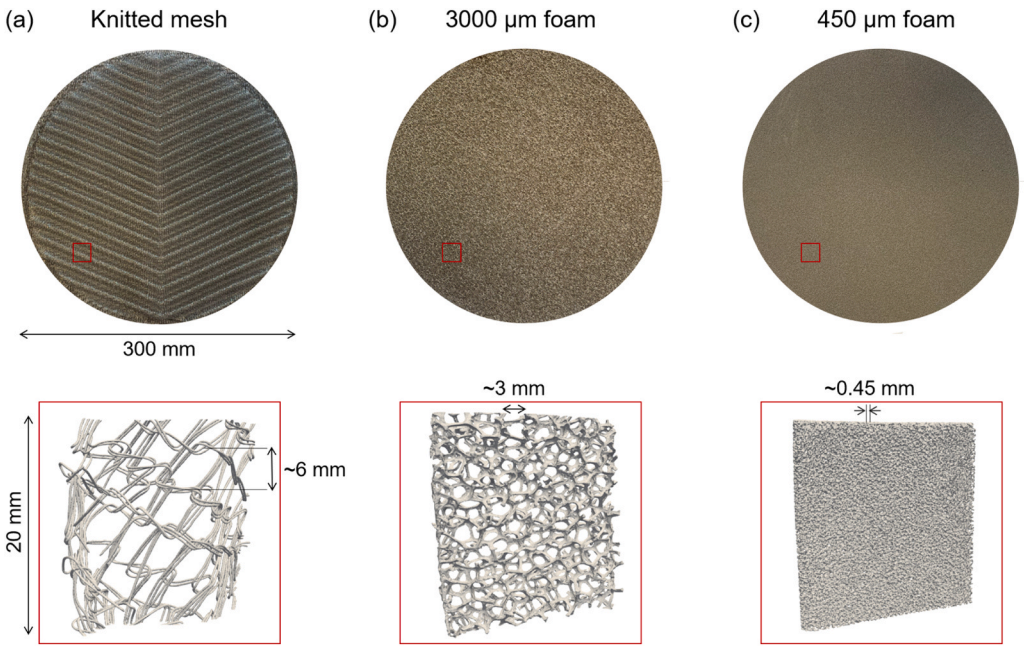


Fig. 3. Optimal micrograph of a circular (a) knitted mesh-type spacer, (b) 3000 µm foam and (c) 450 µm foam used as PTL in prototype AWE electrolysers, with a zoom-in on specific 2 × 2 cm^2 regions, highlighting the difference in pore size.

solution is considered fully converged when this value becomes stationary. This indicates that the overall flow field does not longer change with subsequent iterations. In other words, the present work focuses on stationary solutions. However, given the sudden inlet expansion and the Reynolds numbers involved, Hopf bifurcations may arise, leading to oscillatory behaviour. In such cases, simulations are continued until a statistically stationary regime is reached, while also ensuring that the scaled residuals for the continuity and momentum equations remain below a tolerance of 10^{-5}.

Fig. 2 highlights the details of the final mesh, which is made of 1.7 million elements. A mesh sensitivity analysis has been performed on the cell by monitoring the outlet flow rate as a function of the number of meshing elements. A constant value, close to the theoretical inlet flow rate, is already obtained for 330,000 elements, similarly to [21]. However, since the presence of gas is accounted for in this manuscript, the mesh is voluntarily made finer to capture the local phenomena. The meshing strategy for defining the computational domain consists of a conventional bottom-up approach, in which a CAD model of the cell is used to generate the volume mesh. In a first step, the surface mesh is created by imposing a minimum of 6 cells per gap, i.e. within every narrow geometric region, with a minimum cell size of 0.3 mm and a maximum size of 8 mm. The mesh is considered to be watertight, i.e. fully sealed, and consists of only fluid regions with no voids. Inflation layers are then added to the front wall boundary, i.e. at the electrode surface, so that the zone where the gas is produced is more refined. A poly-hexcore volume mesh, containing polyhedral and hexcore cells, is finally generated.

3. Results and discussion

This section will present the results of our computational framework, consisting of performing multiphase flow simulations on the reference cell configuration presented in Fig. 1. The gas fraction profile within the cell is analysed to assess gas uniformity. Different outlet configurations are then compared as a function of current density to find an optimal configuration for gas evacuation. Finally, the choice of an adequate PTL is discussed.

3.1. Flow behaviour in the reference cell configuration

The reference cell configuration is first investigated in Fig. 4. Fig. 4 (a) shows the mixture velocity profile inside the domain on a plane located at $y = 0$ (see Fig. 2). Electrolyte enters the cell at the inlets and gas is being produced at the electrode surface by imposing a current density j of 2 $A{\cdot}cm^{-2}$ in Eq. (10). As observed, two jet streams develop at the inlets due to the small injection diameters as compared to the larger domain size. These jets coalesce and form one bigger stream that rapidly decreases in intensity within the cell owing to momentum diffusion. This gives rise to some recirculation of the electrolyte and a zone of low velocity (around 0.015 $m{\cdot}s^{-1}$) is observed in the centre of the cell. The flow then accelerates near the top borders of the cell as it approaches the outlets. It appears that the central outlet 3 experiences a higher velocity, and therefore a higher flow rate, as compared to the others. This is already representative of a bad flow distribution among the outlets.

The corresponding gas fraction profile is shown in Fig. 4(b) where it clearly appears that gas accumulates on top of the cell. Indeed, the gas fraction gradually increases from the bottom of the cell, where the electrolyte is being injected, towards the outlets, where the gas-electrolyte mixture is being evacuated. As the gas fraction increases, the mixture density decreases, which reinforces the buoyancy forces and increases the rise velocity of the bubbles as compared to the liquid phase. To assess the impact of j on the gas fraction profile, current densities of 0.2, 0.5 and 1 $A{\cdot}cm^{-2}$ are also tested and the gas fraction at each cell outlet as a function of current density is plotted in Fig. 4(c). Obviously, the gas fraction increases with current density at every outlet. Outlet 3 faces the highest amount of gas, whereas outlets 1 and 2 exhibit lower gas fractions. In other words, the closer to the top, the more gas is evacuated through the outlet channel. The two rightmost outlets (i.e. 4 and 5) present a similar dependence on current density and the corresponding curves in Fig. 4(c) even overlap at low current densities around 0.25 $A{\cdot}cm^{-2}$.

To validate the numerical model used to extract these profiles, one may calculate the theoretical gas fraction expected at the outlet of the cell to verify mass conservation. Knowing the electrolyte inlet flow rate (i.e. 2 × 0.225 $l{\cdot}min^{-1}$) and the gas inlet flow rate, that can be computed based on Eq. (10), the theoretical average outlet gas fraction can be calculated, as a function of current density. This value can be compared

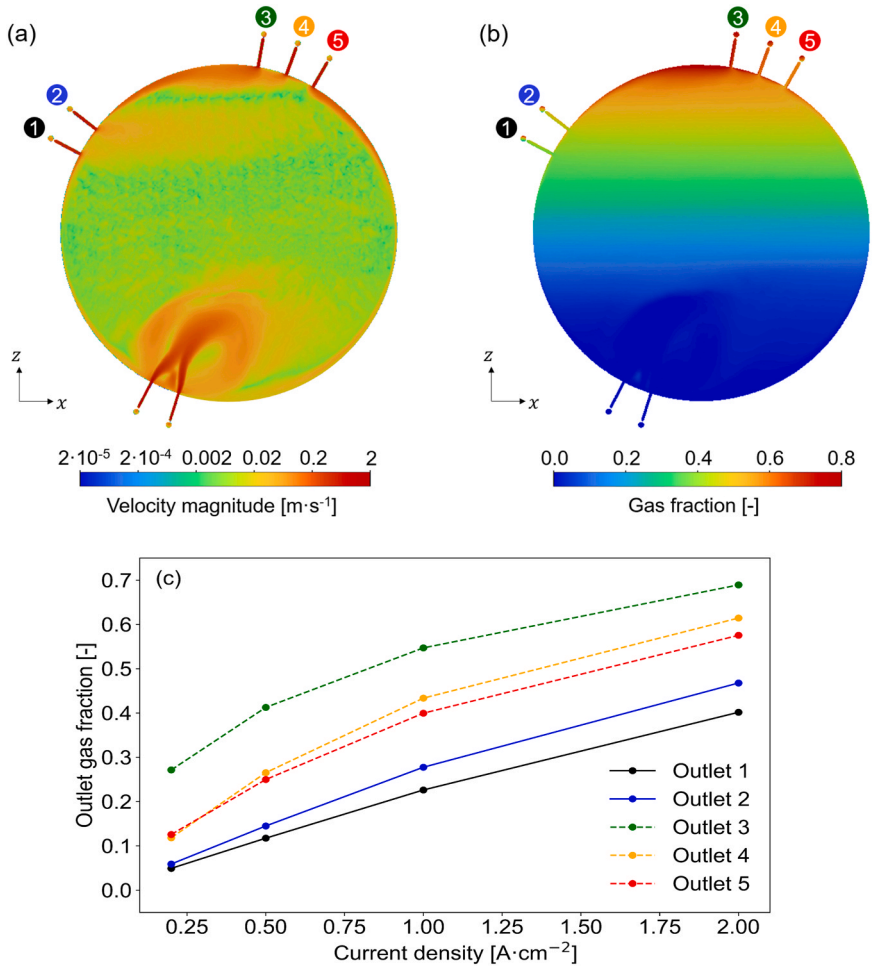


Fig. 4. (a) Mixture velocity profile coloured by magnitude (in log-scale) and (b) gas fraction profile for the reference cell with knitted mesh at a current density of $j = 2$ A·cm^{-2}. The profiles are taken on a plane located at $y = 0$. (c) Outlet gas fraction as a function of current density. An inlet volumetric flow rate of 0.225 l·min^{-1} per inlet is imposed.

to the overall hydrogen volume fraction through the five outlets, extracted from Fig. 4(c), and an estimation of the error on the measure can be obtained. For the considered range of current densities, the relative error remains below 15%, which is totally acceptable. The small discrepancy between theoretical and numerical results can be related to gas bubbles being trapped within the cell, which explains the small mismatch in terms of mass balance.

3.2. Cell design optimisation

In order to find the best configuration in terms of gas evacuation, i.e. the configuration that prevents gas accumulation while homogeneously distributing it through the cell, positioning of the outlet channels is further investigated. At this point, it is important to mention that the cathodic and anodic half-cells are "reversed" within the cell assembly, meaning that the two outlets on the left-hand side of the cathodic compartment will be located on the right-hand side of the anodic half-cell and inversely for the three cathodic outlets on the right. This means that when designing new (half-)cell geometries, the outlets must be positioned so that they do not interfere with the outlet channels of the other compartment. On this basis, three new configurations, denoted A, B and C in Fig. 5(a), are investigated and compared to the reference cell presented previously. Specifically, for configurations A, B and C, outlet 2 is positioned at 40°, 50° and 60°, respectively, while outlet 3 is positioned at 10°, 20° and 30°, respectively. Note that all other geometric parameters (i.e. inlet channels position, inlet and outlet diameters) are kept constant relative to the reference configuration. The gas fraction profiles for these three new designs are shown in Figs. 5(b), 5(c) and 5(d), respectively. As observed, configurations A, B and C present different gas fraction profiles, especially on the top half of the cell, with more gas accumulating as the outlets on the left and on the right go further apart.

To compare different cell configurations quantitatively, a parameter must be defined to assess gas repartition between the outlets. The goal is to have the most homogeneous gas distribution among the outlets, so that each of them is used equally to evacuate the gas. This will go hand in hand with less gas accumulation within the cell. In this respect, a gas outlet uniformity parameter ϕ can be defined as follows:

$$\phi = 1 - \frac{\sqrt{\frac{1}{n}\sum_{i=1}^{n}\left(\alpha_{out,i} - \alpha_{out,\max}\right)^2}}{\alpha_{out,\max}} \tag{13}$$

where n is the number of outlets, $\alpha_{out,i}$ is the gas fraction at outlet i and $\alpha_{out,\max}$ is the maximum outlet gas fraction. Hence, the parameter ϕ takes values from 0 to 1. In the latter case, the standard deviation to the maximum is equal to zero, meaning that the same gas fraction is observed at every outlet, i.e. the gas is uniformly evacuated from the cell.

In Fig. 6, the gas outlet uniformity parameter is calculated for the reference cell configuration and compared to the configurations A, B and C as a function of current density. First of all, it appears that gas is more

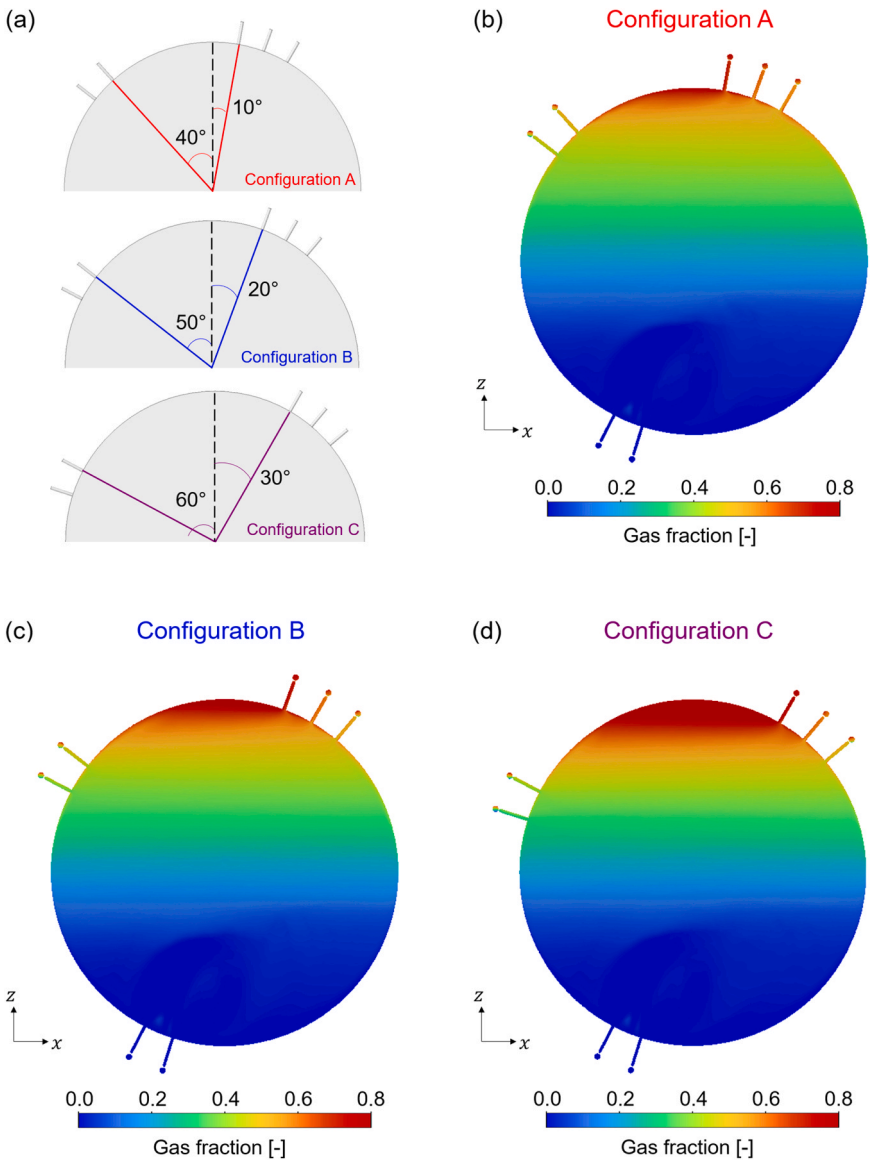


Fig. 5. (a) Outlet configurations compared in this work. Gas fraction profiles for (b) configuration A, (c) configuration B and (d) configuration C with knitted mesh at a current density of $j = 2$ A·cm^{-2}.

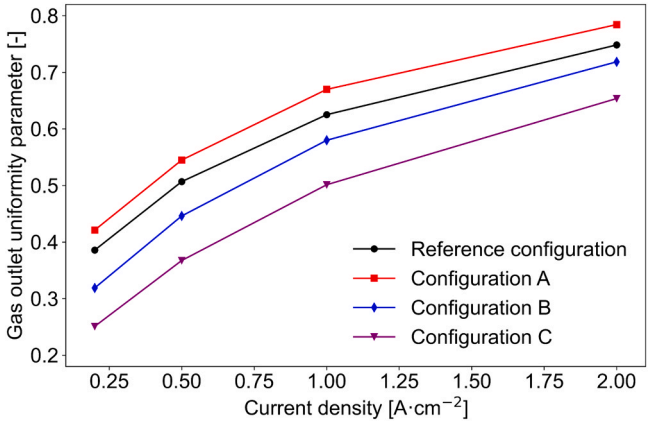


Fig. 6. Gas outlet uniformity parameter as a function of current density for different outlet configurations.

homogeneously distributed among the five outlets (i.e. parameter ϕ increases) for all configurations as current density increases. This trend can be attributed to the increased gas production at higher current densities, which leads to a more complete filling of the cell. Furthermore, the gas outlet uniformity parameter increases when the outlets are closer to the top of the cell (i.e. going from configuration C to A). In comparison to the reference cell design, configuration A presents a slightly better gas uniformity. The only distinction between both designs is the position of the two outlets on the left (located at 40° and 50° for configuration A and the reference cell, respectively), emphasising the importance of placing the outlets closer to the top of the cell, where gas tends to gather. For this reason, and as it also prevents gas accumulation within the cell (see Fig. 5), configuration A appears to be the most promising in order to take advantage of all five outlets. A similar trend is observed when focusing on the outlet flow rate instead of the outlet gas fraction: placing the outlets closer to the top offers a more uniform distribution of flow rate among the outlets. From a practical perspective, maximising the total amount of gas removed from the cell might appear more relevant than simply ensuring a uniform distribution among the five outlets. However, it comes out that both objectives are equivalent in this case since configuration A leads to a maximal gas evacuation, with

an average outlet gas fraction of 0.56 approaching the expected theoretical value of 0.61 as defined in Section 3.1, followed by the reference configuration. Configurations B and C are confirmed to be detrimental from a gas removal point of view. Hence, positioning the outlets at the highest possible point of the cell, i.e. as implemented in configuration A, is optimal for maximising total gas evacuation.

Taking the configuration that gives the highest gas outlet uniformity, we also re-considered the reference design consisting of two outlets placed on the left hand-side of the cell and three of them on the right-hand side. In Fig. 7, the gas outlet uniformity parameter has been plotted for configuration A and for a new configuration, denoted A', where the two left hand-side outlets are shifted towards the right hand-side of the cell, so that all the outlets are on the same side. For low current densities, configuration A with split outlets shows a better utilisation of the five outlets as ϕ is larger as compared to configuration A'. Initially, outlets 1 and 2 were placed apart from outlets 3, 4 and 5 in order to better evacuate gas that would be produced on the left part of the cell. This explains the trend observed in Fig. 7. However, as current density increases, the two curves are closer to each other and similar values of ϕ are reported at $j = 2$ A·cm^{-2}. This highlights that when more gas is produced, every outlet tends to evacuate the same amount of gas and their relative position (split or same-side) does not affect bubble removal anymore. This is confirmed by the gas fraction profiles at high current densities that are quite similar for configurations A and A', emphasising that no more gas accumulates on the left of the cell when same-side outlets (on the right) are considered.

3.3. Selection of the porous transport layer

In this subsection, the choice of the porous transport layer is further investigated. In our previous study [21], single-phase flow simulations were performed to demonstrate that the use of foams as PTL within a prototype electrolyser allows to increase the effective volume covered by the electrolyte while lowering the risk of flow recirculation within the cell. In addition, it was pointed out that the pore size must remain large enough to limit pressure drop across the cell. These observations were verified for the reference cell configuration considered in the present study. As shown in Fig. 8, the use of a coarse 3000 μm foam as PTL instead of a state-of-the-art knitted mesh enables to distribute the flow more homogeneously, without recirculation. However, when analysing the flow repartition among the outlets, it comes out that both types of PTL distribute the electrolyte in a similar and uniform way, with slightly more electrolyte being evacuated through outlets 1 and 2. These results

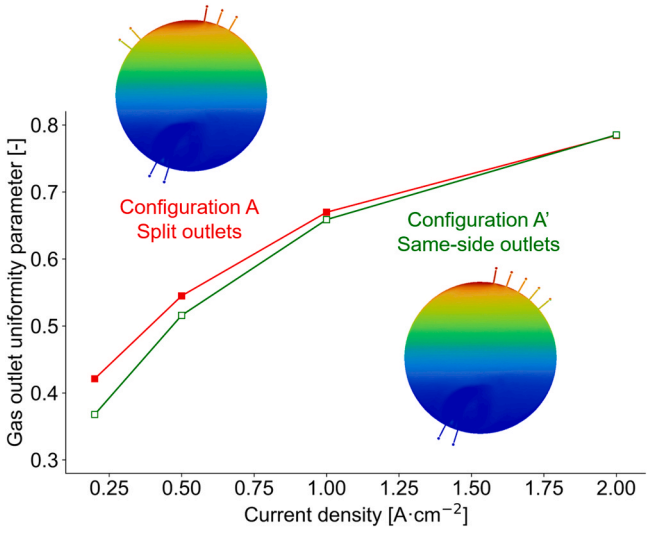


Fig. 7. Gas outlet uniformity parameter as a function of current density, comparing the position of the outlets (split vs same-side).

indicate that single-phase simulations alone are insufficient to draw conclusions regarding gas evacuation.

To better analyse the impact of the PTL on gas distribution and removal, the methodology has been extended to multiphase flow. Fig. 9 compares the gas outlet uniformity parameters of both the reference configuration and of configuration A when using a knitted mesh-type spacer and a 3000 μm foam as PTL. As to the latter, even though the intricated porous structure allows to uniformly spread the electrolyte flow within the cell as shown in Fig. 8(b), the generated gas is not necessarily well-distributed among the five outlets. This results in a lower ϕ parameter as compared to the initial case where a knitted mesh is used as PTL. This is true for both configurations analysed in Fig. 9. This demonstrates the added value of introducing a two-phase model, since differences in gas repartition could not be detected from single-phase simulations. For configuration A though, the cases with knitted mesh and foam are closer than for the reference configuration, emphasising once again that placing the outlets closer to the top of the cell allows for a more uniform gas distribution, independently of the PTL used.

It should be noted that at low current densities, the configurations with knitted mesh and foam are closer to each other in terms of gas outlet uniformity. This means that when less gas is produced, it distributes more easily through the foam towards the outlets. On the contrary, as more gas is produced, it does not spread equally and gas accumulation is prevented when a more open structure like a knitted mesh is used within the cell. This behaviour is confirmed in Fig. 10(a), where a fine 450 μm foam is also considered as PTL in the reference cell configuration. At low current densities, the finer foam even outperforms the knitted mesh in terms of gas outlet uniformity. However, when current density increases, the 450 μm foam evacuates the gas less equally among the outlets as compared to the other (less dense) structures. This can be explained by examining the gas fraction profile within the cell for each type of PTL at a current density of 2 A·cm^{-2}. Fig. 10(b) compares the associated profiles for the reference configuration. When a foam is used as PTL, gas bubbles tend to accumulate more on top of the cell, so that outlet 3 faces a higher gas fraction. This behaviour is even more pronounced when a finer foam is used as PTL. This highlights the fact that this specific design with five outlets is not adapted to the use of a foam as porous transport layer, as gas is not evacuated evenly through the outlets at high current densities.

It is important to remind here that the assumption of a homogeneous gas production on the electrode surface is made, whatever the type of PTL being used. In reality, uniformly injecting the electrolyte inside the cell will lead to a more uniform gas production (taking advantage of the whole electrode surface) and evacuation, which is not necessarily the case when using a knitted mesh-type spacer due to the presence of dead zones [21]. In other words, the quantity of electrogenerated gas might be lower in the latter case compared to what has been considered in this work. This does not substantially change the analysis, except that more stagnant gas will reside in the cell.

4. Conclusion

This work demonstrates how multiphase CFD simulations can be leveraged as a powerful tool to help optimise prototype alkaline water electrolysis cells. A quantitative methodology is proposed to compare different cell configurations through the introduction of a gas outlet uniformity parameter ϕ, which captures the efficiency and homogeneity of gas removal as a function of current density. An optimal configuration is defined as one that prevents gas accumulation while ensuring uniform evacuation from the cell ($\phi \rightarrow 1$). The simulations reveal that gas management is primarily governed by the global cell architecture, with gas preferentially accumulating in the upper region of the cell. Outlet positioning therefore plays a central role in achieving efficient bubble evacuation. For the specific cell geometric dimensions considered in this study, outlets located closer to the top of the cell promote a more ho-

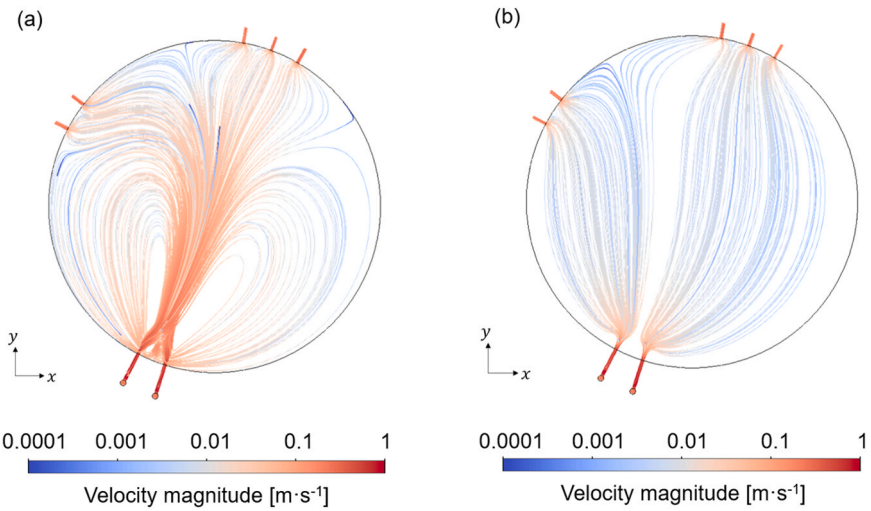


Fig. 8. Velocity streamlines coloured by magnitude (in log-scale) for the reference cell configuration encompassing (a) a knitted mesh-type spacer and (b) a 3000 μm foam as PTL. The results were obtained based on single-phase simulations.

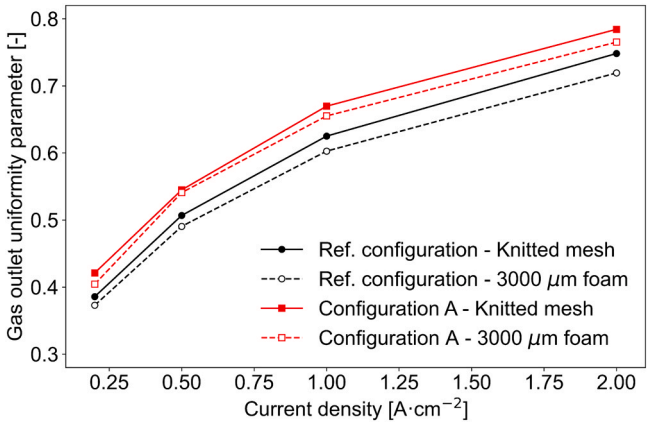


Fig. 9. Gas outlet uniformity parameter as a function of current density, comparing a knitted mesh and a 3000 μm foam as PTL.

mogeneous gas outlet distribution, while splitting outlets on both sides of the cell further improves gas removal, particularly at low current densities. These results highlight that outlet number, location, and spacing strongly govern multiphase transport in AWE cells. Regarding the porous transport layer, our simulations indicate that a knitted mesh promotes more balanced gas outflows than foams within the cell configuration considered in this study, especially at high current densities. The increased gas accumulation observed with the foam does not reflect an intrinsic limitation of this type of PTL, but rather reveals a mismatch between highly porous, tortuous structures and electrolyser geometries originally designed for more open or planar materials. This demonstrates that the present configuration, featuring two inlets and five outlets, is not adapted to fully exploit the advantages of foam-based PTL. More broadly, our findings also suggest that unlocking the full potential of foam-based electrodes and PTL at industrial level will require a paradigm shift in electrolyser design, in which flow fields, gas evacuation pathways, and cell architectures are co-designed. Multiphase CFD emerges as a valuable tool to guide such a more integrated design approach.

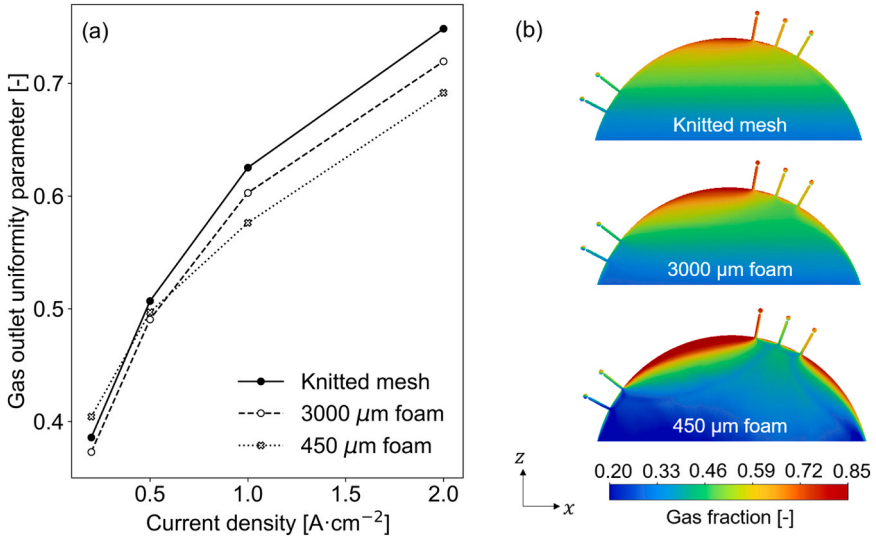


Fig. 10. (a) Gas outlet uniformity parameter as a function of current density comparing different types of PTL in the reference cell configuration. (b) Gas fraction profiles on the top half of the reference cell filled with a knitted mesh-type spacer, a 3000 μm and a 450 μm foam, at a current density of $j = 2$ A·cm^{-2}.

CRediT authorship contribution statement

Kevin Van Droogenbroek: Writing – review & editing, Writing – original draft, Visualization, Validation, Methodology, Investigation, Formal analysis, Data curation. **Ahmed Aissa Berraies:** Software, Methodology. **Hamed Abedini:** Validation, Resources, Project administration. **Benoit Scheid:** Validation. **Joris Proost:** Writing – review & editing, Visualization, Validation, Supervision, Methodology, Funding acquisition.

Declaration of Competing Interest

The authors declare that they have no known competing financial interests or personal relationships that could have appeared to influence the work reported in this paper.

Acknowledgments

Financial support from the Regional Walloon PNRR Project "HeCO2" is gratefully acknowledged. Computational resources have been provided by the supercomputing facilities of the Université catholique de Louvain (CISM/UCL) and the Consortium des Équipements de Calcul Intensif en Fédération Wallonie Bruxelles (CÉCI) funded by the Fond de la Recherche Scientifique de Belgique (F.R.S.-FNRS) under convention 2.5020.11 and by the Walloon Region. B.S is FNRS Research Director.

References

[1] M. Weitzel, J.A. Ordonez, Aligning intermediate climate targets with long-term decarbonisation ambition, npj Clim. Action. 4 (1) (Jul. 2025) 65, https://doi.org/10.1038/s44168-025-00265-y.
[2] IEA, Net Zero by 2050, IEA, Paris, 2021. https://www.iea.org/reports/net-zero-by-2050. Licence: CC BY 4.0.
[3] A. Nurdiawati, I.N. Zaini, W. Wei, R. Gyllenram, W. Yang, P. Samuelsson, Towards fossil-free steel: Life cycle assessment of biosyngas-based direct reduced iron (DRI) production process, J. Clean. Prod. 393 (Mar. 2023) 136262, https://doi.org/10.1016/j.jclepro.2023.136262.
[4] M. Aneke, M. Wang, Energy storage technologies and real life applications – A state of the art review, Appl. Energy 179 (Oct. 2016) 350–377, https://doi.org/10.1016/j.apenergy.2016.06.097.
[5] A.K. Sarker, A.K. Azad, M.G. Rasul, A.T. Doppalapudi, Prospect of green hydrogen generation from hybrid renewable energy sources: a review, Energies 16 (3) (Feb. 2023), https://doi.org/10.3390/en16031556.
[6] T. Wang, X. Cao, L. Jiao, PEM water electrolysis for hydrogen production: fundamentals, advances, and prospects, Carb Neutral. 1 (1) (Jun. 2022) 21, https://doi.org/10.1007/s43979-022-00022-8.
[7] O. Schmidt, A. Gambhir, I. Staffell, A. Hawkes, J. Nelson, S. Few, Future cost and performance of water electrolysis: An expert elicitation study, Int. J. Hydrog. Energy 42 (52) (Dec. 2017) 30470–30492, https://doi.org/10.1016/j.ijhydene.2017.10.045.
[8] M.R. Kraglund, M. Carmo, G. Schiller, S.A. Ansar, D. Aili, E. Christensen, J. O. Jensen, Ion-solvating membranes as a new approach towards high rate alkaline electrolyzers, Energy Environ. Sci. 12 (11) (Nov. 2019) 3313–3318, https://doi.org/10.1039/C9EE00832B.
[9] F. Rocha, R. Delmelle, C. Georgiadis, J. Proost, Effect of pore size and electrolyte flow rate on the bubble removal efficiency of 3D pure Ni foam electrodes during alkaline water electrolysis, J. Environ. Chem. Eng. 10 (3) (June 2022) 107648, https://doi.org/10.1016/j.jece.2022.107648.
[10] F. Rocha, R. Delmelle, C. Georgiadis and J. Proost, Electrochemical Performance Enhancement of 3D Printed Electrodes Tailored for Enhanced Gas Evacuation during Alkaline Water Electrolysis, Advanced Energy Materials, vol. 13, no. 1, p. 2203087, doi: 10.1002/aenm.202203087.
[11] L. Deng, L. Jin, L. Yang, C. Feng, T. An, X. Jia, Z. Geng, C. Zhang, X. Cui, J. Shi, Bubble evolution dynamics in alkaline water electrolysis, eScience 5 (4) (Jul. 2025) 100353, https://doi.org/10.1016/j.esci.2024.100353.
[12] F. Rocha, C. Georgiadis, K. Van Droogenbroek, R. Delmelle, X. Pinon, G. Pyka, G. Kerckhofs, F. Egert, F. Razmjooei, S.A. Ansar, S. Mitsushima, J. Proost, Proton exchange membrane-like alkaline water electrolysis using flow-engineered three-dimensional electrodes, Nat. Commun. 15 (1) (Aug. 2024) 7444, https://doi.org/10.1038/s41467-024-51704-z.
[13] A.Aissa Berraies, K. Van Droogenbroek, G. Pyka, R. Delmelle and J. Proost, Numerical analysis of single-phase electrolyte transport properties in 3D porous electrode structures, Submitted to Chemical Engineering Science.
[14] C. Mansilha, A. Barbosa-Póvoa, L. Tarelho, A. Fonseca, A comprehensive review of green hydrogen production technologies: current status, challenges, research trends and future directions, Renew. Sustain. Energy Rev. 225 (Jan. 2026) 116119, https://doi.org/10.1016/j.rser.2025.116119.
[15] C. Daoudi, T. Bounahmidi, Overview of alkaline water electrolysis modeling, Int. J. Hydrog. Energy 49 (Jan. 2024) 646–667, https://doi.org/10.1016/j.ijhydene.2023.08.345.
[16] M. Bodner, A. Hofer, V. Hacker, H2 generation from alkaline electrolyzer, WIREs Energy Environ. 4 (4) (2015) 365–381, https://doi.org/10.1002/wene.150.
[17] N.P. Sakkas, F. Gillung, K. Thummar, R. Abang, L. Röntzsch, Advanced pressurized alkaline water electrolysis at high temperatures up to 130 °C, Int. J. Hydrog. Energy 149 (Jul. 2025) 150075, https://doi.org/10.1016/j.ijhydene.2025.150075.
[18] G. Hysa, T. Anttilainen, V. Ruuskanen, S. Pöyhönen, A. Kosonen, M. Niemelä, P. Kauranen, J. Ahola, Modelling and Study of Shunt Currents in an Industrial Alkaline Water Electrolyser With Various Number of Cells in Series, IET Renew. Power Gener. 19 (1) (2025) e70112, https://doi.org/10.1049/rpg2.70112.
[19] P. Zhao, J. Wang, W. He, L. Sun, Y. Li, Alkaline zero gap bipolar water electrolyzer for hydrogen production with independent fluid path, Energy Rep. 9 (Oct. 2023) 352–360, https://doi.org/10.1016/j.egyr.2023.05.135.
[20] P. Zhao, J. Wang, L. Sun, Y. Li, H. Xia, W. He, Optimal electrode configuration and system design of compactly-assembled industrial alkaline water electrolyzer, Energy Convers. Manag. 299 (Jan. 2024) 117875, https://doi.org/10.1016/j.enconman.2023.117875.
[21] K. Van Droogenbroek, C. Georgiadis, B. Scheid, J. Proost, Numerical assessment of flow uniformity and recirculation in a water electrolysis cell with knitted mesh and foam-like electrodes, Chem. Eng. Sci. 310 (May 2025) 121513, https://doi.org/10.1016/j.ces.2025.121513.
[22] T. Wang, J. Wang, P. Wang, Z. Ren, X. Yan, W. Wang, W. Guo, Plate structure design guideline for commercial alkaline water electrolyzers (AWEs) with improved liquid flow uniformity: multi-scale quantitative criteria and experimental validation, Int. J. Hydrog. Energy 49 (Jan. 2024) 907–924, https://doi.org/10.1016/j.ijhydene.2023.09.315.
[23] J.C. Koj, C. Wulf, A. Schreiber, P. Zapp, Site-Dependent Environmental Impacts of Industrial Hydrogen Production by Alkaline Water Electrolysis, Energies 10 (7) (Jun. 2017), https://doi.org/10.3390/en10070860.
[24] G. Sakas, A. Ibáñez-Rioja, S. Pöyhönen, L. Järvinen, A. Kosonen, V. Ruuskanen, P. Kauranen, J. Ahola, Sensitivity analysis of the process conditions affecting the shunt currents and the SEC in an industrial-scale alkaline water electrolyzer plant, Appl. Energy 359 (Apr. 2024) 122732, https://doi.org/10.1016/j.apenergy.2024.122732.
[25] L. Xue, S. Song, W. Chen, B. Liu, X. Wang, Enhancing efficiency in alkaline electrolysis cells: optimizing flow channels through multiphase computational fluid dynamics modeling, Art. no. 2, Energies 17 (2) (Jan. 2024), https://doi.org/10.3390/en17020448.
[26] L. Yang, L. Gao, G. Shan, X. Huo, M. Zhang, Y. Wang, X. Liu, A. Kong, J. Wu, J. Zhang, Recent progress of enhanced bubble separation in alkaline water electrolyzer, Chem. Synth. 3 (41) (Sep. 2023), https://doi.org/10.20517/cs.2023.25.
[27] T. Wang, J. Wang, P. Wang, F. Wang, L. Liu, H. Guo, Non-uniform liquid flow distribution in an alkaline water electrolyzer with concave-convex bipolar plate (CCBP): a numerical study, Int. J. Hydrog. Energy (Jan. 2023), https://doi.org/10.1016/j.ijhydene.2022.12.203.
[28] A. Rajora, J.W. Haverkort, An analytical multiphase flow model for parallel plate electrolyzers, Chem. Eng. Sci. 260 (Oct. 2022) 117823, https://doi.org/10.1016/j.ces.2022.117823.
[29] A. Rajora, J.W. Haverkort, An analytical model for the velocity and gas fraction profiles near gas-evolving electrodes, Int. J. Hydrog. Energy 48 (71) (Aug. 2023) 27450–27463, https://doi.org/10.1016/j.ijhydene.2023.03.154.
[30] A. Zarghami, N.G. Deen, A.W. Vreman, CFD modeling of multiphase flow in an alkaline water electrolyzer, Chem. Eng. Sci. 227 (Dec. 2020) 115926, https://doi.org/10.1016/j.ces.2020.115926.
[31] W.A. El-Askary, I.M. Sakr, K.A. Ibrahim, A. Balabel, Hydrodynamics characteristics of hydrogen evolution process through electrolysis: numerical and experimental studies, Energy 90 (Oct. 2015) 722–737, https://doi.org/10.1016/j.energy.2015.07.108.
[32] J. Bai, X. Guan, N. Yang, Three-dimensional CFD simulation of alkaline electrolyzers: flow pattern and electric field, Chem. Eng. J. 515 (Jul. 2025) 163908, https://doi.org/10.1016/j.cej.2025.163908.
[33] M. Dreoni, F. Balduzzi, S.S. Hossain, M. Neben, F.M. Ferro, G. Ferrara, A. Bianchini, Definition of critical metrics for performance evaluation and multiphase flow modeling in an alkaline electrolyzer using CFD, Energies 17 (21) (2024) 5317, https://doi.org/10.3390/en17215317.
[34] W.L. van der Does, N. Valle, J.W. Haverkort, Multiphase alkaline water electrolysis simulations: the need for a solid pressure model to explain experimental bubble overpotentials, Int. J. Hydrog. Energy 102 (Feb. 2025) 295–303, https://doi.org/10.1016/j.ijhydene.2024.12.252.
[35] Crane Co, Flow of Fluids Through Valves, No. 410,. Fittings, and Pipe. Technical Paper, Crane Company, 1988.
[36] M. Ishii, T. Hibiki, Thermo-fluid dynamics of two-phase flow, Springer, New York, NY, 2011, https://doi.org/10.1007/978-1-4419-7985-8.
[37] M. Dreoni, F. Balduzzi, G. Ferrara, A. Bianchini, Accuracy assessment of the eulerian two-phase model for the CFD simulation of gas bubbles dynamics in alkaline electrolyzers, J. Phys. Conf. Ser. 2385 (1) (Dec. 2022) 012040, https://doi.org/10.1088/1742-6596/2385/1/012040.
[38] Y. Liu, S. Li, H. Wu, Y. Shi, Experimental investigation and analysis for the bubble size distribution during alkaline water electrolysis by using a wire electrode, DeCarbon 5 (Sept. 2024) 100052, https://doi.org/10.1016/j.decarb.2024.100052.
[39] P. Van de Velde, B. Scheid, J. Proost, B. Haut, Induced flow and coalescence effects on hydrogen bubble size distribution around a single wire electrode in alkaline

water electrolysis, Chem. Eng. Sci. 311 (Jun. 2025) 121598, https://doi.org/10.1016/j.ces.2025.121598.
[40] J. da Silva, E. Nobrega, F. Staciaki, F.R. Almeida, G. Wosiak, A. Gutierrez, O. Bruno, M.C. Lopes, E. Pereira, Beyond bubbles: Unraveling the interfacial pH effects on bubble size distribution, Chem. Eng. J. 494 (Aug. 2024) 152943, https://doi.org/10.1016/j.cej.2024.152943.
[41] M. Manninen, V. Taivassalo, S. Kallio, On the mixture model for multiphase flow (in VTT Publications), VTT Technical Research Centre of Finland, Espoo, 1996.
[42] Z. Naumann, L. Schiller, A drag coefficient correlation, 318, Z. Ver. Dtsch. Ing. 77 (1935) e323.
[43] A. Hodges, S. Renz, F. Lohmann-Richters, A. Al-Musawi, A. Jupke, W. Lehnert, G. F. Swiegers, G.G. Wallace, Critical analysis of published physical property data for aqueous potassium hydroxide. collation into detailed models for alkaline electrolysis, J. Chem. Eng. Data 68 (7) (Jul. 2023) 1485–1506, https://doi.org/10.1021/acs.jced.3c00040.
[44] N. Zuckerman, N. Lior, Summary, jet impingement heat transfer: physics, correlations, and numerical modeling, Adv. Heat. Transf. 39 (Dec. 2006), https://doi.org/10.1016/S0065-2717(06)39006-5.
[45] F.R. Menter, Two-equation eddy-viscosity turbulence models for engineering applications, AIAA J. 32 (8) (Aug. 1994) 1598–1605, https://doi.org/10.2514/3.12149.
[46] S. Whitaker, The Forchheimer equation: a theoretical development, Transp. Porous Med. 25 (1) (Oct. 1996) 27–61, https://doi.org/10.1007/BF00141261.
[47] D. Edouard, M. Lacroix, C.P. Huu, F. Luck, Pressure drop modeling on SOLID foam: state-of-the art correlation, Chem. Eng. J. 144 (2) (Oct. 2008) 299–311, https://doi.org/10.1016/j.cej.2008.06.007.
[48] D. Le Bideau, P. Mandin, M. Benbouzid, M. Kim, M. Sellier, Review of necessary thermophysical properties and their sensivities with temperature and electrolyte mass fractions for alkaline water electrolysis multiphysics modelling, Int. J. Hydrog. Energy 44 (10) (Feb. 2019) 4553–4569, https://doi.org/10.1016/j.ijhydene.2018.12.222.